RSC Advances

PAPER

View Article Online
View Journal | View Issue

Cite this: *RSC Adv.*, 2026, **16**, 27837

Mechanistic study of structural regulation and enhanced oxygen reduction performance in $La_{0.5}Sr_{1.5}FeO_{4+\delta}$ cathodes *via* Mg doping

Yanpeng Liu,[a] Songbo Li, *[a] Shengli An,[b] Hongli Qiao,[a] Yuanyaun Ma,[a] Jia Xu,[cd] Jing Zhang,[a] Xu Zhang[a] and Jianlin Zhao[a]

Received 11th April 2026
Accepted 18th May 2026

DOI: 10.1039/d6ra03050e

rsc.li/rsc-advances

To develop high-performance cathode materials for intermediate-temperature solid oxide fuel cells (IT-SOFCs), this study systematically investigated how magnesium doping regulates the structure and electrochemical performance of $La_{0.5}Sr_{1.5}FeO_{4+\delta}$ (LSF). A series of $La_{0.5}Sr_{1.5}Fe_{1-x}Mg_xO_{4+\delta}$ samples ($LSFM_x$; $x = 0$, 0.025, 0.050, 0.075, and 0.100) were synthesized by the sol–gel method. XRD, XPS, SEM, and TEM results confirmed that Mg^{2+} was successfully incorporated into the LSF lattice, which promoted the formation of oxygen vacancies and effectively lowered the thermal expansion coefficient, thereby improving thermal compatibility with the electrolyte. Electrochemical measurements showed that moderate Mg doping ($x = 0.050$) markedly enhanced the oxygen reduction reaction (ORR) activity of the cathode. At 800 °C, the corresponding single cell delivered a peak power density of 0.60 W cm^{-2}, representing a 36% increase over the undoped sample, and also exhibited excellent long-term operational stability. Combined distribution of relaxation times (DRT) analysis and first-principles calculations further revealed that Mg doping improves the reversibility of oxygen migration pathways and lowers the oxygen dissociation energy barrier, thereby enhancing interfacial oxygen transport and surface exchange kinetics. These results provide an effective strategy and deeper theoretical insight for designing high-performance, highly stable SOFC cathodes through cation doping.

1 Introduction

Solid oxide fuel cells (SOFCs) are an efficient and clean energy-conversion technology. Because of their high energy-conversion efficiency, fuel flexibility, and environmental friendliness, they have shown strong potential for applications in distributed power generation and sustainable energy systems.[1] However, the commercialization of SOFCs still faces major challenges, including high cost and limited service life. In particular, the sluggish oxygen reduction reaction kinetics of cathode materials under intermediate-temperature operation (600–800 °C) remains one of the key bottlenecks limiting further improvements in cell performance.[2,3] Therefore, developing cathode materials with high catalytic activity, excellent electronic conductivity, and good thermal stability is of great importance for advancing SOFC technology.[4]

LSF materials with a Ruddlesden–Popper structure have attracted considerable attention because of their distinctive layered framework and high structural stability.[5] However, they still suffer from insufficient oxygen reduction activity and a mismatch in thermal expansion coefficient relative to the electrolyte. In recent years, tuning material properties through B-site cation doping has become a major research focus. Among the available dopants, Mg is particularly attractive because of its stable valence state, low cost, and ability to modify the lattice.[6] Previous studies have shown that partial substitution of Fe by Mg^{2+} can effectively promote the formation of oxygen vacancies and improve thermal compatibility between the electrode and the electrolyte.[7] Nevertheless, systematic studies on the microstructural evolution, electrochemical regulation mechanisms, and thermal–stability pathways of Mg-doped LSF cathodes remain limited. In particular, the quantitative relationship between doping level and oxygen reduction kinetics still requires further clarification.

Accordingly, this work prepared a series of $La_{0.5}Sr_{1.5}Fe_{1-x}Mg_xO_{4+\delta}$ samples ($x = 0$, 0.025, 0.050, 0.075, and 0.100) by partially substituting B-site Fe with Mg^{2+}. The effects of Mg doping on the crystal structure, oxygen nonstoichiometry, impedance behavior, ORR catalytic activity, and thermal expansion were then systematically investigated. In addition, EIS and DRT analyses were combined to clarify how Mg doping

[a]*College of Chemistry and Chemical Engineering, Inner Mongolia University of Science & Technology, Baotou 014010, China. E-mail: lisongbo@imust.edu.cn*
[b]*College of Rare Earth Industry, Inner Mongolia University of Science and Technology, Baotou 014010, China*
[c]*School of Rare Earth Industry, Inner Mongolia University of Science and Technology, Baotou 014010, China*
[d]*Analysis and Testing Center, Inner Mongolia University of Science and Technology, Baotou 014010, China*

influences ORR activity. By integrating XRD, SEM, TEM, EPR, power-density testing, long-term stability evaluation, thermal-expansion measurements, and first-principles calculations, this study aims to reveal the microscopic role of partial Mg substitution and the pathway responsible for performance enhancement, thereby providing both experimental evidence and theoretical support for the development of high-performance R–P-type cobalt-free cathodes. Overall, this work not only deepens the understanding of how Mg doping improves LSF cathodes, but also offers useful guidance for the design of high-performance, long-life cathode materials for intermediate-temperature SOFCs, with clear significance for the commercialization of SOFC technology.[8,9]

2 Experimental section

2.1 Synthesis of cathode materials

A series of layered perovskite oxides, $La_{0.5}Sr_{1.5}Fe_{1-x}Mg_xO_{4+\delta}$ ($LSFM_x$; $x = 0$, 0.025, 0.050, 0.075, and 0.100), were synthesized by an optimized ethylenediaminetetraacetic acid (EDTA)–citric acid (CA) sol–gel route. Analytical-grade $La(NO_3)_3\cdot 6H_2O$, $Sr(NO_3)_2$, $Fe(NO_3)_3\cdot 9H_2O$, and $Mg(NO_3)_2\cdot 6H_2O$ were used as the metal precursors, while EDTA and CA served as dual complexing agents. The molar ratio of total metal cations to EDTA to CA was fixed at 1 : 1 : 1.5. The pH of the precursor solution was adjusted to 7–8 with aqueous ammonia under continuous stirring. The solution was then heated at 80 °C in a thermostatic water bath with vigorous stirring until a homogeneous viscous gel formed. The gel was pre-calcined at 250 °C for 5 h to remove organic species, followed by final calcination at 1100 °C for 5 h in air to obtain phase-pure $LSFM_x$ powders.

2.2 Fabrication of electrochemical cells

Symmetric cells: $Sm_{0.2}Ce_{0.8}O_{1.9}$ (SDC) electrolyte disks (12 mm in diameter) were uniaxially pressed at 10 MPa and sintered at 1450 °C for 10 h to obtain dense, gas-tight electrolytes. A cathode slurry was prepared by dispersing $LSFM_x$ powder in an organic vehicle composed of ethyl cellulose and camphor alcohol (mass ratio 96 : 4) at a solid loading of 50 wt%. The mixture was thoroughly ball-milled to ensure homogeneity. The slurry was then screen-printed onto both sides of the SDC electrolyte disks, dried at 80 °C, and co-sintered at 1100 °C for 5 h to form symmetric cells with the configuration $LSFM_x$|SDC|$LSFM_x$.

Anode-supported single cells: NiO-YSZ (8 mol% Y_2O_3-stabilized ZrO_2) anode supports were prepared by tape casting followed by controlled thermal decomposition. A slurry containing NiO, YSZ, and starch (mass ratio 12 : 8 : 5) was ball-milled, cast into green tapes, and laminated. Sequential dry pressing was then used to deposit the NiO-YSZ anode functional layer, the YSZ electrolyte layer, and the $Gd_{0.1}Ce_{0.9}O_{1.9}$ (GDC) barrier layer. The multilayer green body was uniaxially pressed at 10 MPa and sintered at 1450 °C for 5 h to obtain a dense half-cell with the configuration NiO-YSZ|YSZ|GDC. The $LSFM_x$ cathode slurry was subsequently screen-printed onto the GDC surface and sintered at 1100 °C for 5 h to complete the full cell with the configuration NiO-YSZ|YSZ|GDC|$LSFM_x$.

2.3 Characterization and performance evaluation

Phase identification and quantitative phase analysis were performed by XRD (Malvern Panalytical B.V., Cu Kα radiation, $\lambda = 1.5418$ Å) over a 2θ range of 10–80° at a scan rate of 5° min^{-1}. Rietveld refinement was performed using GSAS-II/EXPGUI software. Microstructural features, including grain morphology, lattice fringes, and elemental distributions, were examined by high-resolution transmission electron microscopy (HR-TEM; JEOL JEM-2100F) equipped with energy-dispersive X-ray spectroscopy (EDS). Cross-sectional microstructures and elemental maps of the fabricated cells were obtained by field-emission scanning electron microscopy (FE-SEM; TESCAN GAIA3) coupled with EDS. Surface chemical states were analyzed by XPS (Thermo Scientific ESCALAB 250Xi), with all binding energies referenced to the C 1s peak at 284.8 eV. The linear thermal expansion coefficients (TECs) of bulk $LSFM_x$ pellets were measured from 30 to 800 °C in an N_2 atmosphere using a dilatometer (NETZSCH DIL 402C) at a heating rate of 5 °C min^{-1}. Electrochemical impedance spectroscopy (EIS) measurements were performed on symmetric cells in static air from 600 to 800 °C using an electrochemical workstation (Metrohm Autolab PGSTAT302). The frequency range was 0.1 Hz to 100 kHz with an AC perturbation amplitude of 10 mV. Distribution of relaxation times (DRT) analysis was used to separate the polarization processes. For single-cell testing, a custom-built fixture was employed. Humidified hydrogen (3 vol% H_2O in H_2, 50 mL min^{-1}) was supplied to the anode, while the cathode was exposed to static air. Current–voltage (*I–V*) and current–power (*I–P*) curves were recorded from 600 to 800 °C. Long-term stability was evaluated by constant-current polarization at 650 °C and 0.3 A cm^{-2} for up to 100 h on the best-performing cell.

2.4 Density Functional Theory (DFT) calculation methods and parameters

Before calculations, bulk structure of $La_9Sr_{27}Fe_{18}O_{63}$ was built based on $LaSrFeO_4$ primitive cell. Number of oxygen vacancies were determined by ratio of Fe^{2+} and Fe^{3+} in $La_9Sr_{27}Fe_{18}O_{63}$(Fe^{2+} : Fe^{3+} = 1 : 1). Bulk structure of $La_9Sr_{27}Fe_{17}Mg_1O_{63}$ was built by replacing Fe^{2+} with Mg^{2+} in $La_9Sr_{27}Fe_{18}O_{63}$. Sr-exposed and SrLa-exposed $La_9Sr_{27}Fe_{18}O_{63}$ (100) unitcell with one stoichiometric layer were built based on $La_9Sr_{27}Fe_{18}O_{63}$ bulk structure. Sr-terminated $La_9Sr_{27}Fe_{17}Mg_1O_{63}$ (100) unitcell with one stoichiometric layer was built based on $La_9Sr_{27}Fe_{17}Mg_1O_{63}$ bulk structure. In slab model, thickness along *c* direction was set at 30 Å to avoid weak interactions between images.

In the Density Functional Theory (DFT) calculations, structural optimization was performed using the Vienna *Ab initio* Simulation Package (VASP) with the projector augmented wave (PAW) method. The exchange–correlation functional was treated with the Perdew–Burke–Ernzerhof (PBE) functional[10] combined with the DFT-D3 correction.[11] The cut-off energy of

the plane-wave basis was set to 450 eV for structural optimization. For optimization of the lattice parameters, Brillouin-zone integration was performed using a Monkhorst–Pack *k*-point mesh of 0.04 $Å^{-1}$. The self-consistent calculations employed an energy convergence threshold of 10^{-5} eV. The equilibrium geometries and lattice constants were optimized with the maximum stress on each atom constrained to 0.02 eV $Å^{-1}$. Spin polarization was included to describe the magnetic properties of the models. Specifically, equal and opposite magnetic moments were assigned to Ni atoms to represent antiferromagnetism in the models. The Hubbard *U* correction was applied to the 3d orbitals of Fe and Cu and the 5d orbitals of La, with $U_{Fe} = 4.0$ eV, $U_{Cu} = 4.0$ eV, and $U_{La} = 5.4$ eV.[12] Transition states and O-atom migration paths were determined using the climbing image nudged elastic band (CINEB) method.

In the CINEB calculations, the energy criterion and stress criterion were set to 10^{-7} eV and 0.05 eV $Å^{-1}$, respectively.

The segregation energy from the bulk structure to the Sr-exposed and LaSr-exposed slab models was defined as E_s. $E_s = [E\text{ (surface)} - E\text{ (bulk)}]/S$. Here, E (surface) represents the total energy of the slab model with a given exposed termination, E (bulk) represents the total energy of the bulk structure, and S represents the surface area of the slab model with the corresponding exposed termination.

The dissociation energy of O_2 was defined as E_d. $E_d = E(\text{Ov–}O_2) - E(\text{Ov–O–O})$. Here, $E(\text{Ov–}O_2)$ represents the total energy of the oxygen-vacancy-containing slab model with O_2 adsorbed on the surface, whereas E(Ov–O–O) represents the total energy of the oxygen-vacancy-containing slab model with dissociated O atoms adsorbed on the surface.

3 Results and discussion

3.1 Phase and microstructural characterization

3.1.1 XRD analysis and Rietveld structural refinement. To determine the crystal structure of the samples, X-ray diffraction (XRD) measurements were performed on $LSFM_x$ ($x = 0$, 0.025, 0.050, 0.075, and 0.100), and the results are presented in Fig. 1(a and b). All diffraction patterns match the standard card for $LaSrFeO_4$ (PDF# 71-1745), indicating that all samples crystallize in a single-phase R–P structure with a tetragonal *I*4/*mmm* (No. 139) space group. No new diffraction peaks appeared after Mg doping. As the Mg content increased, the XRD peaks gradually shifted toward lower angles. The refinement results further showed a gradual increase in unit-cell volume with increasing Mg content. The refined patterns of LSF and $LSFM_{0.050}$ are shown in Fig. 1(c and d), and the detailed refinement results are summarized in Table 1. The regular shift of diffraction peaks together with the continuous variation of lattice parameters in Table 1 demonstrates a systematic lattice evolution induced by Mg substitution.

Excellent high-temperature chemical compatibility between the cathode and the electrolyte is essential for the long-term stable operation of solid oxide fuel cells. To verify this property, $LSFM_{0.050}$ was uniformly mixed with SDC and GDC electrolyte powders at a mass ratio of 1 : 1 and then calcined in air at 1100 °C for 10 h to simulate possible interfacial reactions during cell fabrication and high-temperature operation. The XRD patterns of the calcined mixtures are shown in Fig. 1(p and q). Only the diffraction peaks of $LSFM_{0.050}$, SDC, and GDC were observed, with no impurity phases or obvious peak shifts. These results indicate that no significant chemical reaction occurred between $LSFM_{0.050}$ and either SDC or GDC during the high-temperature treatment, demonstrating good thermochemical compatibility and providing a basis for the long-term reliable operation of the cell.

Combined with ionic radius matching, lattice expansion behavior, and the regular change of Fe valence as well as oxygen vacancy content (3.1.3), it can be rationally confirmed that Mg^{2+} preferentially occupies the Fe B-site of R–P lattice, and all samples still maintain pure single-phase structure even at high doping levels.

3.1.2 Electron microscopy and elemental distribution analysis. Analysis of the fast Fourier transform (FFT) and inverse FFT images (Fig. 1(h) and (n)) showed that the interplanar spacing of the (222) plane was 0.28 nm. Compared with the standard LSF PDF card, this spacing is slightly larger, which is consistent with the XRD refinement results and further indicates that Mg doping increases the unit-cell volume.[13] In addition, the EDS surface-scanning results (Fig. 1(i–m)) show that Mg, La, Sr, Fe, and O are uniformly distributed throughout the material, suggesting that Mg was successfully incorporated into the lattice. The elemental proportion plot in Fig. 1(o) is also in good agreement with the theoretical composition, further confirming the successful incorporation of Mg into the LSF lattice.

The microscopic morphologies and elemental distributions of the symmetric cells and single cells were further examined by scanning electron microscopy (SEM). Fig. 1(r–v) shows cross-sectional SEM images of the symmetric cells based on $LSFM_x$ ($x = 0$, 0.025, 0.050, 0.075, and 0.100), Fig. 1(w) shows the cross-section of the single cell, and Fig. 1(i–m) presents the EDS maps of $LSFM_{0.050}$. The elemental distributions are relatively uniform, and the electrolyte layer is dense, which is beneficial for O^{2-} transport.[14] By contrast, the cathode is porous and loose, which increases the contact area with oxygen and facilitates oxygen conversion at the cathode surface as well as charge transfer.[15] The cathode also maintains intimate contact with the electrolyte, with no obvious delamination. This behavior is attributed to the TEC of $LSFM_x$ being close to that of SDC, which helps ensure efficient O^{2-} and charge transport during cell operation.[16]

3.1.3 Surface chemical state and electronic structure (XPS/EPR) analysis. The influence effect of Mg doping on the surface chemical states of LSF was investigated by X-ray photoelectron spectroscopy (XPS). Fig. 2(c) shows the XPS survey spectra of the $LSFM_x$ series, in which the characteristic peaks of La, Sr, Fe, Mg, and O are clearly visible, confirming the successful incorporation of Mg into the LSF cathode. Fig. 2(a) presents the Fe 2p spectra and the corresponding peak-fitting results. The peaks at 709.3–710.2 eV and 723.1–723.9 eV are assigned to Fe^{2+}, whereas those at 710.3–711.2 eV and 726.2–727.4 eV are attributed to Fe^{3+}.[17,18] These results indicate the coexistence of Fe^{2+} and Fe^{3+} in $LSFM_x$. As summarized in Table 2, the Fe^{3+}/Fe^{2+} ratio

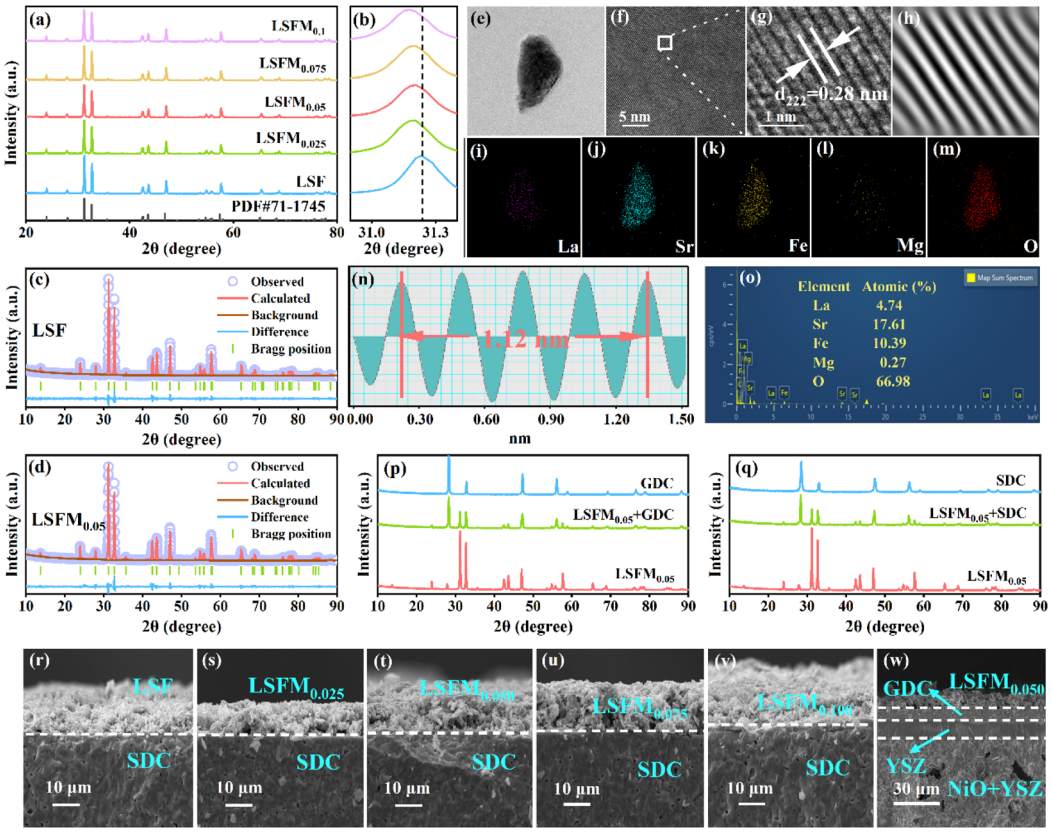

Fig. 1 (a) X-ray diffraction (XRD) pattern of $LSFM_x$; (b) enlarged view of the low-angle region in (a); (c and d) Rietveld-refined XRD patterns of LSF and $LSFM_{0.050}$; (e) transmission electron microscopy (TEM) image of $LSFM_{0.050}$; (f) high-resolution TEM (HR-TEM) image of the rectangular region marked in (e); (g) magnified HR-TEM image of the selected area in (f); (h) inverse fast Fourier transform (IFFT) image derived from the lattice fringes in (g); (i–m) energy-dispersive X-ray spectroscopy (EDS) elemental maps of $LSFM_{0.050}$ for La, Sr, Fe, Mg, and O; (n) line-profile IFFT analysis across a representative grain boundary in $LSFM_{0.050}$; (o) quantitative elemental distribution profile obtained *via* EDS point analysis; (p and q) XRD patterns of the calcined (1100 °C, 5 h) composites $LSFM_{0.050}$–SDC and $LSFM_{0.050}$–GDC, respectively; (r–v) scanning electron microscopy (SEM) images of a symmetric cell employing $LSFM_x$ as the cathode; (w) cross-sectional SEM image of a single solid oxide fuel cell (SOFC) with the configuration $LSFM_{0.050}$|GDC|YSZ|NiO–YSZ.

gradually decreases with increasing Mg content, suggesting that Mg doping promotes the partial reduction of Fe^{3+} to Fe^{2+}, which is favorable for charge compensation and oxygen-vacancy formation.[19] According to the quantitative Fe^{2+}/Fe^{3+} ratios from XPS and charge balance principle, the oxygen vacancy content (δ) was calculated and listed in Table 2. Combined with the EPR results, it further confirms the increased oxygen vacancies with Mg doping. Based on the XPS-derived Fe^{2+}/Fe^{3+} ratios and charge-balance calculated oxygen vacancy content (δ) in Table 2, a clear quantitative correlation can be established: Mg doping induces the reduction of Fe^{3+} to Fe^{2+}, increases oxygen vacancy concentration, and thereby optimizes the ORR kinetic process of the cathode material.

Fig. 2(b) shows the fitted O 1s spectra. The low-binding-energy peak at 528.7–529.2 eV corresponds to lattice oxygen (O_{lat}), whereas the high-binding-energy peak at 530.9–531.4 eV is associated with surface-adsorbed oxygen (O_{ads}).[20,21] As listed in Table 2, the relative content of O_{ads} increases gradually with increasing Mg content, indicating that Mg doping promotes oxygen adsorption and thereby further enhances the ORR activity of $LSFM_x$.

Fig. 2(d) presents the electron paramagnetic resonance (EPR) spectra of the $LSFM_x$ series. All samples show clear EPR signals

Table 1 XRD refined data of $LSFM_x$ material

Sample	Crystal system	Space group	a (Å)	b (Å)	c (Å)	Vol (Å^3)	R_{wp} (%)	χ^2
LSF	Tetragonal	$I4/mmm$ (139)	3.839	3.839	12.659	186.599	9.994	1.49
$LSFM_{0.025}$	Tetragonal	$I4/mmm$ (139)	3.842	3.842	12.674	187.051	8.776	1.23
$LSFM_{0.050}$	Tetragonal	$I4/mmm$ (139)	3.842	3.842	12.675	187.117	9.349	1.29
$LSFM_{0.075}$	Tetragonal	$I4/mmm$ (139)	3.842	3.842	12.678	187.138	9.982	1.43
$LSFM_{0.100}$	Tetragonal	$I4/mmm$ (139)	3.842	3.842	12.689	187.289	9.968	1.45

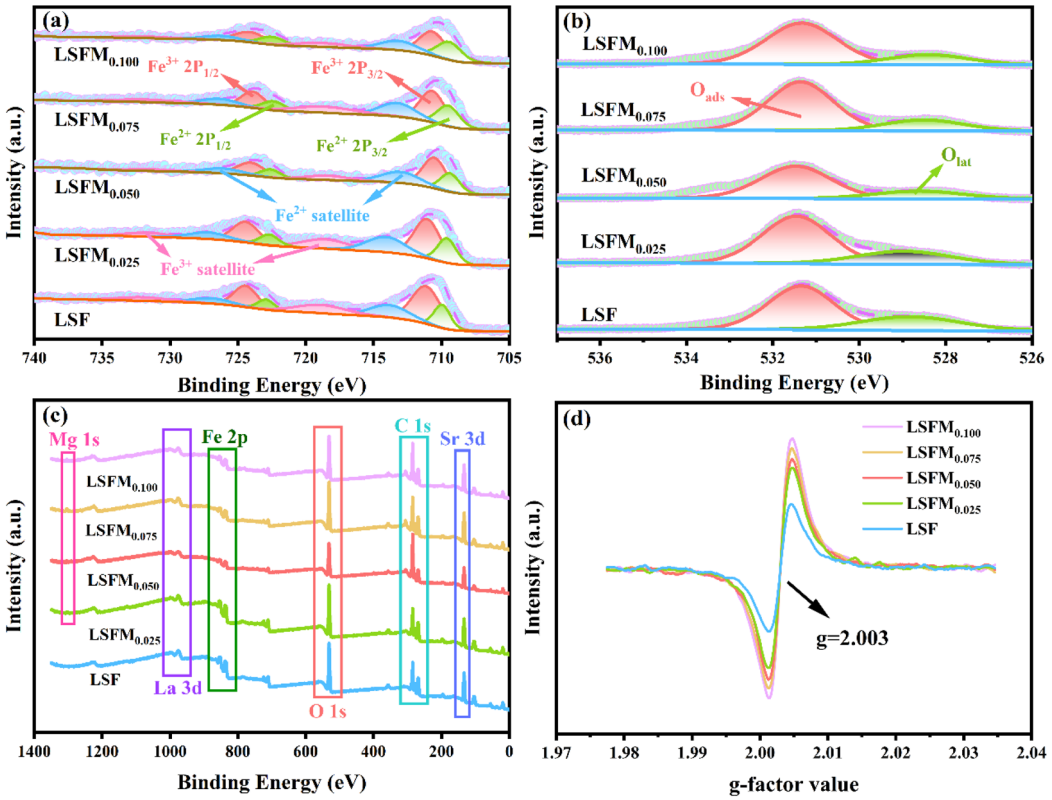

Fig. 2 XPS curve of LSFMx: (a) Fe 2p; (b) O 1s; (c) XPS spectra of all elements; (d) EPR diagram.

Table 2 Fitting results of O 1s and Fe 2p peaks for $LSFM_x$ cathodes, and calculated oxygen nonstoichiometry (δ) (All percentages are in %; δ is dimensionless)

Sample	O_{ads}	O_{lat}	Fe^{3+}	Fe^{2+}	Fe^{2+}/Fe^{3+}	δ
LSF	67.57	32.43	66.43	33.57	0.50	0.08
$LSFM_{0.025}$	72.08	27.92	61.23	38.77	0.63	0.11
$LSFM_{0.050}$	76.43	23.57	58.92	41.08	0.69	0.13
$LSFM_{0.075}$	77.88	22.12	54.45	45.55	0.83	0.16
$LSFM_{0.100}$	78.34	21.66	50.35	49.65	0.98	0.19

near $g = 2.003$, which are attributed to paramagnetic centers associated with oxygen vacancies.[22] Quantitative analysis of the signal intensity shows that the intensity increases markedly as the Mg^{2+} doping level rises, indicating that the concentration of oxygen vacancies also increases. This result is consistent with the XPS results, which show a decreasing Fe^{3+}/Fe^{2+} ratio and an increasing O_{ads} content in the O 1s spectra. Taken together, these findings confirm that Mg doping effectively promotes oxygen-vacancy formation and thus provides favorable structural conditions for enhancing the oxygen reduction activity of the material.

The oxygen vacancy content indicated by XPS fitting and EPR results further verifies the inherent relationship among Mg doping, lattice defect evolution, and oxygen migration behavior, providing quantitative support for the proposed ORR mechanism regulation pathway.

3.2 Evaluation of electrochemical and thermo-mechanical performance

3.2.1 Electrochemical impedance spectroscopy (EIS) and distribution of relaxation times (DRT) analysis. Symmetric cells with the configuration $LSFM_x|SDC|LSFM_x$ were prepared to evaluate the ORR activity of $LSFM_x$ through electrochemical impedance spectroscopy (EIS). The EIS data of the symmetric cells were collected in air over the temperature range of 600–800 °C. The spectra measured at 600–800 °C were further analyzed by DRT to obtain the distribution of relaxation times. The ORR process of $LSFM_x$ was separated into three characteristic frequency regions corresponding to different physicochemical processes. Generally, the low-frequency (LF) process is dominated by gas-phase oxygen adsorption, dissociation and surface diffusion on the cathode surface.[23] The intermediate-frequency (IF) response mainly originates from oxygen surface exchange and interfacial charge-transfer kinetics of the electrode.[24] The high-frequency (HF) process is primarily attributed to oxygen ion migration and interfacial polarization at the cathode–electrolyte contact boundary.[25] The fitted peak area in each frequency interval represents the corresponding impedance contribution.

This frequency-domain assignment of relaxation processes follows the widely recognized DRT interpretation principle for layered Ruddlesden–Popper cathodes reported in the literature.

Fig. 3(a) shows the DRT fitting curves of $LSFM_x$ ($x = 0$, 0.025, 0.050, 0.075, and 0.100) at 800 °C. The spectra are dominated by

the HF contribution, indicating that oxygen transport at the cathode/SDC interface is the rate-limiting step under this condition. Compared with undoped LSF, the Mg-doped samples exhibit significantly smaller HF and IF peak areas at 800 °C. Moreover, as the Mg content increases, the HF peak area first decreases and then increases, reaching a minimum at $x = 0.050$. This result demonstrates that appropriate Mg doping optimizes the interfacial oxygen transport and electrode reaction kinetics. The relatively small LF peak area implies favorable low-frequency oxygen reaction behavior of the as-prepared material.

Within the temperature range of 600 °C to 800 °C, the HF peak area of $LSFM_{0.050}$ decreases markedly as the temperature rises (Fig. 3(b)). This behavior is mainly attributed to the enhanced mobility of oxygen ions at higher temperature and the accelerated oxygen-exchange reaction at the electrode/electrolyte interface, both of which reduce interfacial transport resistance.[26] The IF peaks associated with charge transfer also decrease with increasing temperature, further confirming the positive effect of thermal activation on electrode kinetics.

Based on the DRT results, the EIS data were fitted using the equivalent circuit L-R_S-(R_{HF}-CPE_{HF})-(R_{IF}-CPE_{LF})-(R_{LF}-CPE_{LF}), where R_{HF}, R_{IF}, and R_{LF} represent the impedance contributions generated by the HF, IF, and LF electrode processes identified in the DRT analysis. According to the fitting results, the polarization resistance R_P ($R_P = R_{HF} + R_{IF} + R_{LF}$) can be obtained. To compare the EIS behavior of $LSFM_x$ more clearly, Fig. 3(c) and (d) show the fitted EIS curves of LSF and $LSFM_{0.050}$, respectively, over the temperature range of 600–800 °C. Fig. 3(e) shows the ASR values of $LSFM_x$ ($x = 0$, 0.025, 0.050, 0.075, and 0.100) in the same temperature range, and the corresponding numerical values are listed in SI Table S1. The introduction of Mg lowers the ASR values relative to the LSF matrix. As the Mg content increases, the ASR of $LSFM_x$ first decreases and then increases, reaching a minimum at $x = 0.050$. At 800 °C, the ASR of $LSFM_{0.050}$ is 0.087 Ω cm^2, which is approximately 57% lower than that of undoped LSF, indicating that Mg doping effectively enhances the catalytic performance of the electrode.

Fig. 3(f) shows the Arrhenius plots of the R_p values of symmetric cells with the configuration $LSFM_x$|SDC|$LSFM_x$ as a function of temperature. The activation energy E_a of the ORR can be obtained from the slope of the fitted line.[27] It is evident that Mg doping significantly decreases E_a, indicating that Mg incorporation positively promotes the ORR activity of LSF.

Notably, conventional EIS-DRT alone cannot strictly decouple surface oxygen exchange kinetics from bulk oxygen diffusion. Unambiguous distinction requires additional specialized characterization, so this work only discusses the overall polarization relaxation behavior without excessive mechanistic separation.

3.2.2 Thermal expansion behavior and electrolyte compatibility. Fig. 4(a) shows the thermal-expansion curves of the $LSFM_x$ series ($x = 0$, 0.025, 0.050, 0.075, and 0.100) over the temperature range of 30–800 °C. To suppress chemical expansion caused by oxygen loss and to make the measured results more representative of the intrinsic thermal-expansion behavior of the materials, all tests were conducted in an N_2

Atmosphere, the heating rate was set at 2 °C min^{-1}. The average thermal expansion coefficient (TEC) of each sample is listed in the figure.

Compared with undoped LSF, Mg doping markedly lowers the average TEC. When the Mg doping content $x = 0.025$, 0.050, 0.075, and 0.100, the average TEC values of $LSFM_x$ in the range of 30–800 °C are 16.52 × 10^{-6} K^{-1}, 14.96 × 10^{-6} K^{-1}, 14.33 × 10^{-6} K^{-1}, and 13.87 × 10^{-6} K^{-1}, respectively. As the Mg content increases, the TEC of $LSFM_x$ decreases gradually. Over the

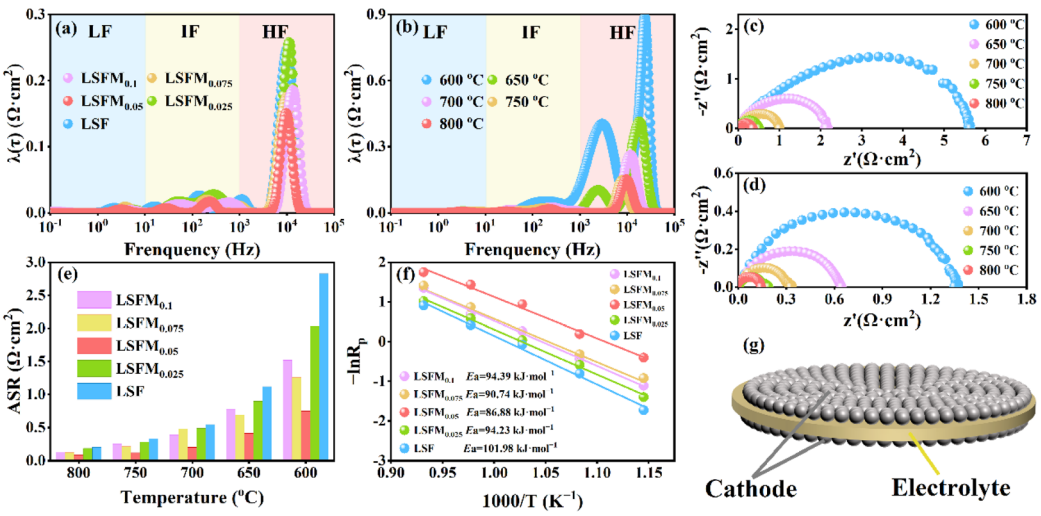

Fig. 3 (a) Impedance relaxation spectra of $LSFM_x$ measured at 800 °C; (b) temperature-dependent impedance relaxation spectra of $LSFM_{0.050}$ over the range of 600–800 °C; (c) polarization resistance (R_p) *versus* temperature for the symmetrical LSF|SDC|LSF cell under ambient air atmosphere; (d) polarization resistance (R_p) *versus* temperature for the symmetrical $LSFM_{0.050}$|SDC|$LSFM_{0.050}$ cell under ambient air atmosphere; (e) area-specific resistance (ASR) values of $LSFM_x$ across 600–800 °C; (f) Arrhenius plot of the bulk ionic conductivity of $LSFM_x$ in the temperature range of 600–800 °C; (g) schematic illustration of the symmetrical solid oxide cell configuration.

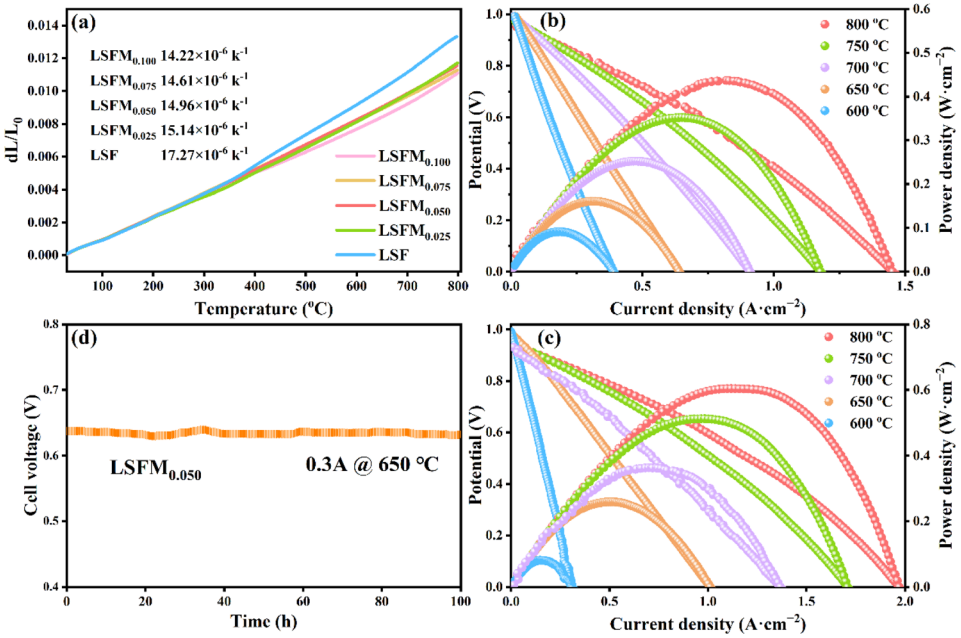

Fig. 4 (a) Thermal expansion curve of $LSFM_x$ material at temperatures ranging from 30–800 °C; (b) *I–P–V* curve of LSF at temperatures ranging from 600 to 800 °C; (c) *I–P–V* curve of $LSFM_{0.050}$ at temperatures ranging from 600–800 °C; (d) stability test of an anode-supported single cell of $LSFM_{0.050}$ under conditions of 0.3 A cm^{-2} and 650 °C.

temperature range of 30–800 °C, the average TEC of $LSFM_{0.050}$ is 14.96 × 10^{-6} K^{-1}, which is about 13% lower than that of the undoped sample and closer to that of the commonly used electrolyte SDC (12.74 × 10^{-6} K^{-1}). This result indicates that an appropriate amount of Mg doping can effectively improve the thermal-expansion matching between LSF and the electrolyte. The lower TEC can be mainly attributed to the stabilizing effect of Mg^{2+} on the lattice. Partial substitution of Fe by Mg^{2+} suppresses changes in the Fe valence state and the accompanying loss of lattice oxygen at high temperature, thereby reducing the extra expansion caused by nonstoichiometric variation.[31] In addition, the Mg–O bond (about 400 kJ mol^{-1}) generally has a higher bond energy than the Fe–O bond (about 300–350 kJ mol^{-1}), which helps increase lattice rigidity and further suppress thermal expansion at high temperature.[32] Therefore, by regulating the Mg content, the thermal-expansion behavior of $LSFM_x$ cathodes can be effectively tailored, thereby improving their structural compatibility with the electrolyte during thermal cycling.

3.2.3 Single-cell electrochemical performance and operational stability. The anode-supported single cell NiO-YSZ|YSZ|GDC|$LSFM_x$ was mounted in the test fixture, and a high-temperature-resistant sealing material was uniformly applied at the junction between the single cell and the alumina tube to ensure good gas tightness. During testing, humidified hydrogen containing 5% H_2O was introduced to the anode as the fuel, while the cathode was exposed to air as the oxidant. All single-cell measurements were conducted with identical electrode fabrication and testing protocols, ensuring the validity and comparability of the obtained electrochemical results. Power-density measurements were carried out from 600 to 800 °C, and the data were collected during the cooling process. Fig. 4(b) and (c) show the power-density curves of undoped LSF and Mg-doped $LSFM_{0.050}$, respectively, from 600 to 800 °C. The results show that the peak power density of $LSFM_{0.050}$ reaches 0.60 W cm^{-2} at 800 °C, which is about 36% higher than that of undoped LSF, confirming that Mg doping can effectively improve the output performance of the single cell. Detailed electrochemical performance comparisons with recently reported state-of-the-art Ruddlesden–Popper cathode materials under similar operating temperatures are summarized in Table 3, further confirming the competitive ASR and peak power density of the optimal $LSFM_{0.050}$ cathode.

A stability test was further conducted on the NiO-YSZ|YSZ|GDC|$LSFM_{0.050}$ single cell at 650 °C under a constant current density of 0.3 A cm^{-2} for 100 h. The results are shown in Fig. 4(d). Throughout the entire test period, the cell voltage remained stable without obvious attenuation, indicating that $LSFM_{0.050}$ has excellent long-term operational stability as a cathode material for intermediate-temperature solid oxide fuel cells. It is acknowledged that the current 100 h continuous operation test is relatively limited; long-term durability

Table 3 Comparison of ASR and PPD for Ruddlesden–Popper (R–P) type oxide electrodes

Sample	ASR	PPD
$La_{1.8}Sr_{0.2}NiO_{4+\delta}$ (ref. 28)	0.41 Ω cm^2	0.52 W cm^{-2}
$La_{1.5}Ba_{0.5}NiO_{4+\delta}$ (ref. 29)	0.127 Ω cm^2	0.51 W cm^{-2}
$La_2Ni_{0.9}Sc_{0.1}O_{4+\delta}$ (ref. 30)	0.129 Ω cm^2	0.46 W cm^{-2}
$La_{0.5}Sr_{1.5}Fe_{1.95}Mg_{0.05}O_{4+\delta}$	0.087 Ω cm^2	0.60 W cm^{-2}

evaluation exceeding 500 h will be performed in our follow-up study to further verify practical application potential.

3.3 DFT calculations and reaction mechanism study

After structural optimization, the segregation energies from bulk LSF and $LSFM_{0.050}$ to the Sr-exposed LSF (100) and $LSFM_{0.050}$ (100) surfaces were calculated, as shown in Fig. 5(a) and (b). The results show that the segregation energy of the Sr-exposed LSF surface is 1.919 J m^{-2}, whereas that of $LSFM_{0.050}$ increases slightly to 1.930 J m^{-2}. Thus, Mg doping leads to a small increase in the Sr segregation energy, by approximately 0.5%.

Based on the O-IS and O-FS structures of oxygen vacancies in each system, the $*O_2$ and *O–O adsorption configurations were constructed, as shown in Fig. 5(c and d). After structural optimization, the dissociation energies from $*O_2$ to *O–O were calculated, and the optimized structures were denoted as *Ov–O_2 and *Ov–O–O. The results indicate that the O_2 dissociation energy is approximately −1.64 eV for undoped LSF and approximately −1.78 eV for $LSFM_{0.050}$. This suggests that Mg doping can effectively enhance oxygen adsorption, thereby increasing the surface oxygen-exchange rate and ultimately improving ORR catalytic activity.

Furthermore, first-principles calculations were used to systematically analyze the oxygen-migration energy barriers on the Sr-exposed (100) surface. The forward energy barrier was defined as the absolute difference between the transition-state energy and the initial-state energy, whereas the reverse energy barrier was defined as the absolute difference between the transition-state energy and the final-state energy. The migration of oxygen atoms was visualized by marking the migrating oxygen atoms with differently colored spheres, as shown in Fig. 5(e) and (f). The migration-energy-barrier profiles of O atoms on LSF and $LSFM_{0.050}$ are presented in Fig. 5(g). The calculated energy barriers for each elementary migration step are summarized in Table S2, while the oxygen vacancy formation energies are presented in Table S3.

The calculation results show that the undoped LSF surface has an extremely low forward migration barrier of only 0.07 eV, but a reverse migration barrier as high as approximately 1.44 eV. This pronounced asymmetry between the forward and reverse barriers implies that once oxygen atoms migrate to the final state, they can scarcely return to the initial position, indicating poor reversibility of this migration pathway and limited oxygen-migration activity. In contrast, for Mg-doped $LSFM_{0.050}$, the forward and reverse migration barriers are approximately 0.59 eV and 0.81 eV, respectively, giving a difference of only 0.22 eV. In this study, oxygen migration reversibility is defined as the bidirectional migration ability of oxygen ions between the cathode surface and bulk lattice. This result indicates that Mg doping improves the surface migration activity of oxygen atoms and makes the migration pathway much more reversible.

After Mg doping, the oxygen dissociation energy decreases from −1.64 eV to −1.78 eV, indicating that the oxygen molecular dissociation process becomes more thermodynamically favorable upon Mg substitution. This behavior originates from the local charge compensation and structural distortion induced by Mg^{2+} substitution at the Fe site. With a fixed valence state and lower electronegativity, the introduced Mg^{2+} modulates the covalency and electronic structure of surrounding Fe–O bonds, which facilitates the formation and stabilization of surface oxygen vacancies and further enhances the activation capability of the material toward oxygen molecules.

In terms of oxygen migration barriers, the increase in the forward migration barrier and the decrease in the reverse migration barrier of $LSFM_{0.05}$ reveal that Mg doping does not simply reduce the overall barrier of all migration pathways; instead, it reconstructs the potential energy surface for oxygen

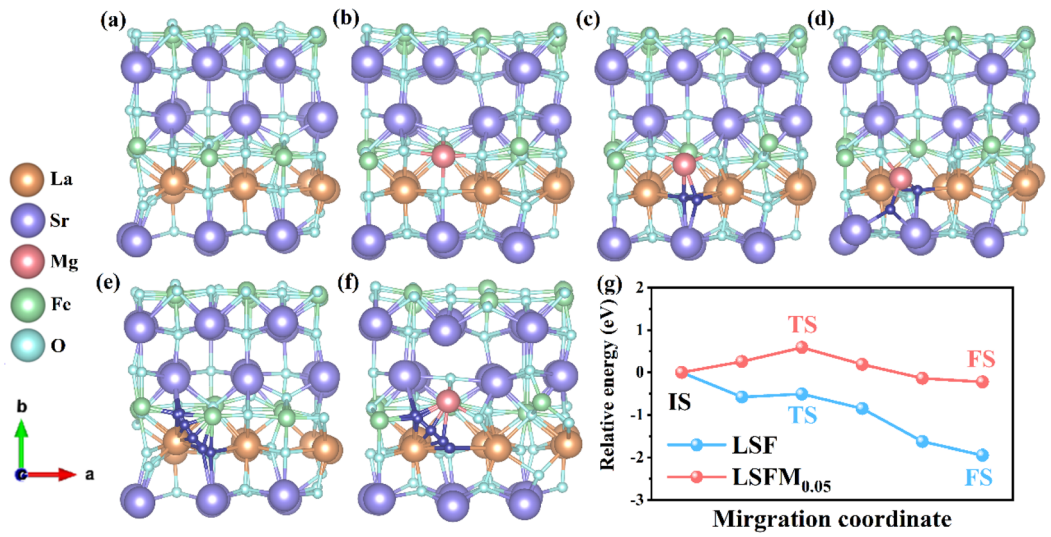

Fig. 5 (a) Crystal cell model diagram of LSF; (b) crystal cell model diagram of $LSFM_{0.050}$; (c) *Ov–O_2 diagram of Sr-exposed $LSFM_{0.050}$; (d) *Ov–O–O diagram of Sr-exposed $LSFM_{0.050}$; (e) oxygen atom migration path diagram of Sr-exposed LSF; (f) oxygen atom migration path diagram of Sr-exposed $LSFM_{0.050}$; (g) migration energy barrier diagram of O atoms on Sr-exposed LSF and $LSFM_{0.050}$.

vacancy migration. The region adjacent to Mg acts as a relatively stable site for oxygen vacancies, leading to a reduced energy barrier when oxygen vacancies migrate toward this region, while a higher barrier is required for vacancies migrating outward from this area. Accordingly, the obvious reduction of the reverse migration barrier from 1.44 eV to 0.81 eV can be reasonably explained by this mechanism.

Overall, Mg doping optimizes O_2 adsorption and oxygen migration at multiple levels. Such a synergistic mechanism is not a simple incremental conclusion, but a quantitatively verified regulation rule derived from multi-characterization and theoretical calculation. Enhanced O_2 adsorption can increase the surface oxygen-exchange rate, while the more balanced migration-energy barriers give the oxygen-migration process higher reversibility and more favorable kinetics. These effects work synergistically and are therefore expected to significantly improve the ORR catalytic performance of the material.

4 Conclusions

This study systematically investigated how Mg doping influences the structure, electrochemical performance, and thermal stability of $La_{0.5}Sr_{1.5}FeO_{4+\delta}$ (LSF) cathodes. XRD, XPS, SEM, and TEM results confirmed that Mg^{2+} was successfully incorporated into the LSF lattice to form a single-phase R–P structure with a uniform elemental distribution. Mg doping caused lattice expansion and simultaneously promoted the partial reduction of Fe^{3+} to Fe^{2+}, thereby increasing the concentration of oxygen vacancies and providing more active sites for the ORR. Electrochemical measurements showed that appropriate Mg doping can significantly enhance ORR catalytic activity. At 800 °C, the ASR of $LSFM_{0.050}$ was about 57% lower than that of undoped LSF, while the peak power density increased by 36%. DRT analysis further demonstrated that Mg doping effectively reduced the impedance contributions in the HF region (oxygen transport at the cathode/electrolyte interface) and the IF region (surface charge transfer), thereby improving oxygen-ion migration and surface oxygen-exchange kinetics. First-principles calculations further confirmed at the atomic scale that Mg doping lowers the oxygen dissociation energy from −1.64 eV to −1.78 eV and improves the reversibility of oxygen migration by reducing the reverse energy barrier from 1.44 eV to 0.81 eV, thus providing theoretical support for the observed performance enhancement. The thermal-expansion results show that Mg doping reduces the TEC from about $17.2 \times 10^{-6}\ K^{-1}$ to $14.96 \times 10^{-6}\ K^{-1}$, thereby significantly improving thermal compatibility with the SDC electrolyte. Combined with the stable voltage observed during the 100 h stability test, these results indicate that $LSFM_{0.050}$ combines excellent electrochemical performance with long-term operational stability. By integrating structural characterization, electrochemical evaluation, and theoretical calculations, this study demonstrates that appropriate Mg doping effectively enhances the overall performance of LSF-based cathodes through multiple mechanisms, including lattice regulation, oxygen-vacancy generation, and improved interfacial transport kinetics. These findings provide useful guidance for the design of cathode materials for intermediate-temperature solid oxide fuel cells.

Author contributions

Yanpeng Liu: writing – original draft, investigation, data curation. Songbo Li: funding acquisition, methodology, review & editing. Shengli An: supervision. Hongli Qiao: data curation, investigation. Yuanyaun Ma: data curation, investigation. Jia Xu: formal analysis. Jing Zhang: formal analysis. Xu Zhang: validation. Jianlin Zhao: data curation.

Conflicts of interest

There are no conflicts to declare.

Data availability

The data that support the findings of this study are available from the corresponding author upon reasonable request.

Supplementary information (SI) is available. See DOI: https://doi.org/10.1039/d6ra03050e.

Acknowledgements

This work was supported by the Natural Science Foundation of Inner Mongolia Autonomous Region (2025LHMS02014), the Inner Mongolia Autonomous Region Universities Basic Scientific Research Project (2023CXPT002), the Inner Mongolia Autonomous Region Key R&D and Achievement Transformation Program Projects (2025YFDZ0005), the Integrated Research Platform of Novel and Important Energy Comprehensive Utilization Technology in Inner Mongolia Autonomous Region and the Open Project of Rare Earth Advanced Materials Technology Innovation Center (CXZX–D–202409–0020).

Notes and references

1 F. G. Venegas, M. Petit and Y. Perez, Active integration of electric vehicles into distribution grids: Barriers and frameworks for flexibility services, *Renewable Sustainable Energy Rev.*, 2021, **145**, 111060.

2 L. S. Mahmud, A. Muchtar and M. R. Somalu, Challenges in fabricating planar solid oxide fuel cells: A review, *Renewable Sustainable Energy Rev.*, 2017, **72**, 105–116.

3 D. S. Dhawale, S. Biswas, G. Kaur, *et al.*, Challenges and advancement in direct ammonia solid oxide fuel cells: a review, *Inorg. Chem. Front.*, 2023, **10**(21), 6176–6192.

4 O. Corigliano, L. Pagnotta and P. Fragiacomo, On the technology of solid oxide fuel cell (SOFC) energy systems for stationary power generation: a review, *Sustainability*, 2022, **14**(22), 15276.

5 S. Qu, Z. Song, J. Gong, *et al.*, Feasibility of proton-conducting solid oxide fuel cell equipped with cobalt-doped Fe-based RP phase cathode for application in mine air environment, *J. Rare Earths*, 2025, DOI: 10.1016/j.jre.2025.12.033.

6 C. L. Chang, C. H. Tsai, C. S. Yang, *et al.*, Fabrication and electrochemical performance of reversible metal-supported solid oxide cells *via* atmospheric plasma spraying, *Electrochim. Acta*, 2025, **536**, 146727.
7 Y. Ye, Y. Ding, H. Yang, *et al.*, Boosting near-infrared emission in spinel-type phosphor *via* oxygen vacancy engineering for versatile application, *Adv. Funct. Mater.*, 2024, **34**(42), 2405048.
8 K. Hu, B. Li, Z. Tian, *et al.*, Multiscale Simulation in Fuel Cell and Electrolyzer Systems: a Review of Methods, Applications, and Future Prospects, *Sustainable Engineering Novit*, 2025, **1**, 5.
9 Y. Su, G. Yuan, J. Hu, *et al.*, Thiosalicylic-acid-mediated coordination structure of nickel center *via* thermodynamic modulation for aqueous Ni–Zn batteries, *Adv. Mater.*, 2024, **36**(32), 2406094.
10 J. Hafner, Ab-initio simulations of materials using VASP: density-functional theory and beyond, *J. Comput. Chem.*, 2008, **29**(13), 2044–2078.
11 S. Grimme, Semiempirical GGA-type density functional constructed with a long-range dispersion correction, *J. Comput. Chem.*, 2006, **27**(15), 1787–1799.
12 H. Jiang, Revisiting the GW approach to d-and f-electron oxides, *Phys. Rev. B*, 2018, **97**(24), 245132.
13 M. A. Short and Jr P. L. Walker, Measurement of interlayer spacings and crystal sizes in turbostratic carbons, *Carbon*, 1963, **1**(1), 3–9.
14 H. Lee, D. J. Lee, M. Kim, *et al.*, High-energy density Li–O_2 battery with a polymer electrolyte-coated CNT electrode *via* the layer-by-layer method, *ACS Appl. Mater. Interfaces*, 2020, **12**(15), 17385–17395.
15 H. Wang, X. Wang, M. Li, *et al.*, Porous materials applied in nonaqueous Li–O_2 batteries: status and perspectives, *Adv. Mater.*, 2020, **32**(44), 2002559.
16 Y. Dou, Z. Xie, Y. Wei, *et al.*, Redox mediators for high-performance lithium–oxygen batteries, *Natl. Sci. Rev.*, 2022, **9**(4), nwac040.
17 D. Liang, Y. Lu, L. Hu, *et al.*, Mesoporous $TiNb_2O_7$ nanosheets anode with excellent rate capability and cycling performance in lithium ion half/full batteries, *J. Power Sources*, 2022, **544**, 231897.
18 T. Chen, G. Wei, S. Jiang, *et al.*, Enhanced resistance to helium irradiations through unusual interaction between high-entropy-alloy and helium, *Scr. Mater.*, 2023, **224**, 114328.
19 R. Liu, Y. Zhang, L. Duan, *et al.*, Effect of Fe^{2+}/Fe^{3+} ratio on photocatalytic activities of $Zn_{1-x}Fe_xO$ nanoparticles fabricated by the auto combustion method, *Ceram. Int.*, 2020, **46**(1), 1–7.
20 X. Hu, J. Wang, J. Wang, *et al.*, β particles induced directional inward migration of oxygen vacancies: surface oxygen vacancies and interface oxygen vacancies synergistically activate PMS, *Appl. Catal., B*, 2022, **318**, 121879.
21 X. Li, J. Feng, N. Sun, *et al.*, A-Site High-Entropy Engineering of Oxygen Electrode: A Promising Route to Durable and Active Reversible Solid Oxide Cells, *Adv. Mater.*, 2026, e21863.
22 Z. Zhao, Y. Mi, S. Wang, *et al.*, The high p*K*a-guided defect engineering: improving fluoride removal in actual scenarios by benzimidazole modulated metal–organic frameworks, *Water Res.*, 2025, **280**, 123510.
23 X. Peng, H. Shen, K. Su, *et al.*, Stable and fast ion transport electrolyte interfaces modified with novel fluorine-and nitrogen-containing solvents for Ni-rich cathode materials, *ACS Appl. Mater. Interfaces*, 2024, **16**(26), 34281–34293.
24 J. Cabana, B. J. Kwon and L. Hu, Mechanisms of degradation and strategies for the stabilization of cathode–electrolyte interfaces in Li-ion batteries, *Acc. Chem. Res.*, 2018, **51**(2), 299–308.
25 H. Chen, H. Zhang, Y. Zhou, *et al.*, Structure-conduction correlations in a chlorine-rich superionic lithium-argyrodite solid electrolyte: a DRT analysis, *J. Power Sources*, 2023, **583**, 233579.
26 Q. Wang, Y. Gu, W. Zhu, *et al.*, Noble-metal-assisted fast interfacial oxygen migration with topotactic phase transition in perovskite oxides, *Adv. Funct. Mater.*, 2021, **31**(50), 2106765.
27 R. Kumar, V. Yadav, P. Singh, *et al.*, Effect of calcination temperature on the structural, microstructure, and electrical properties of CeO_2 nanoparticles as a solid electrolyte for IT-SOFC application, *Adv. Powder Technol.*, 2024, **35**(12), 104710.
28 Y. P. Wang, Q. Xu, D. P. Huang, *et al.*, Evaluation of $La_{1.8}Sr_{0.2}NiO_{4+\delta}$ as cathode for intermediate temperature solid oxide fuel cells, *Int. J. Hydrogen Energy*, 2016, **41**(15), 6476–6485.
29 X. Wu, C. Gu, J. Cao, *et al.*, Investigations on electrochemical performance of $La2NiO_{4+\delta}$ cathode material doped at A site for solid oxide fuel cells, *Mater. Res. Express*, 2020, **7**(6), 065507.
30 H. Gong, D. Zhou, X. Zhu, *et al.*, Characterization of B-Site Sc-doped $La_2Ni_{1-x}Sc_xO_{4+\delta}$ (x = 0, 0.05, 0.10, and 0.15) perovskites as cathode materials for IT-SOFCs, *Int. J. Hydrogen Energy*, 2024, **50**, 1492–1502.
31 E. Boivin, R. A. House, J. J. Marie, *et al.*, Controlling iron *versus* oxygen redox in the layered cathode $Na_{0.67}Fe_{0.5}Mn_{0.5}O_2$: mitigating voltage and capacity fade by Mg substitution, *Adv. Energy Mater.*, 2022, **12**(30), 2200702.
32 D. Triyono, U. Hanifah and H. Laysandra, Structural and optical properties of Mg-substituted $LaFeO_3$ nanoparticles prepared by a sol–gel method, *Results Phys.*, 2020, **16**, 102995.